Electrocatalytic Oxygen Reduction

Direct Oxygen-Oxygen Cleavage through Optimizing Interatomic Distances in Dual Single-atom Electrocatalysts for Efficient Oxygen Reduction Reaction

Yuhan Xie[+], Xin Chen[+], Kaian Sun, Jinqiang Zhang,* Wei-Hong Lai,* Hao Liu,* and Guoxiu Wang*

Abstract: The oxygen reduction reaction (ORR) on transition single-atom catalysts (SACs) is sustainable in energy-conversion devices. However, the atomically controllable fabrication of single-atom sites and the sluggish kinetics of ORR have remained challenging. Here, we accelerate the kinetics of acid ORR through a direct O–O cleavage pathway through using a bi-functional ligand-assisted strategy to pre-control the distance of hetero-metal atoms. Concretely, the as-synthesized Fe–Zn diatomic pairs on carbon substrates exhibited an outstanding ORR performance with the ultrahigh half-wave potential of 0.86 V vs. RHE in acid electrolyte. Experimental evidence and density functional theory calculations confirmed that the Fe–Zn diatomic pairs with a specific distance range of around 3 Å, which is the key to their ultrahigh activity, average the interaction between hetero-diatomic active sites and oxygen molecules. This work offers new insight into atomically controllable SACs synthesis and addresses the limitations of the ORR dissociative mechanism.

Introduction

Electrochemical reduction of molecular oxygen is an essential reaction for fuel cells and metal-air batteries.[1] However, the oxygen reduction reaction (ORR) using high-efficiency and low-cost electrocatalysts is a bottleneck in these energy devices.[2] One strategy is to develop nonprecious metal catalysts (NPMCs) with low mass-loading metals to substitute noble-metal catalysts.[3] In the 1960s, Jasinski discovered that cobalt phthalocyanine (CoPc) with four nitrogen-coordinated (Co–N_4) active centers could catalyze ORR.[4] Several macrocyclic organics, which have the structure of four N-coordinated metals (M–N_4) like iron (Fe)–N_4 and Co–N_4, have been developed as first-generation NPMCs.[5] However, the poor electronic conductivity and instability of these organic M–N_4 species limited their ORR performance.[6] In the 2010s, carbon-based single-atom catalysts (SACs) with similar M-N_x structures attracted tremendous interest due to their low cost and good electrochemical performance in the field of energy-related electrocatalysis, including ORR.[7] Since these single atoms (SAs) are engineered in a highly conductive and stable carbon framework, the major issues of M–N_4 macrocycle complexes have been overcome. Moreover, the tuneable electronic structure and unsaturated coordination environment of SAs offer opportunities to develop efficient ORR catalysts.[8]

Many experimental and theoretical investigations have been devoted to elucidating the electrocatalytic mechanism of ORR. Three oxygen adsorption models have been proposed. They are the end-on adsorption (Pauling model), the bridge model (Yeager model), as shown in Figure 1a, and the on-top adsorption (Griffiths model) (Figure S1).[9] The generalized four-electron ORR mechanism in acid media has been widely recognized and is preceded by either

[*] Y. Xie,[+] Dr. J. Zhang, Prof. H. Liu, Prof. G. Wang
Center for Clean Energy Technology, School of Mathematical and Physical Science, Faculty of Science, University of Technology Sydney
Sydney, New South Wales 2007 (Australia)
E-mail: jinqiang.zhang@utoronto.ca
Hao.Liu@uts.edu.au
Guoxiu.Wang@uts.edu.au

Dr. X. Chen[+]
Beijing Advanced Innovation Center for Materials Genome Engineering, Institute of Solid State Chemistry, University of Science and Technology Beijing
Beijing 100083 (China)

Dr. K. Sun
Department of Chemistry, Tsinghua University
Beijing 100084 (China)

Dr. W.-H. Lai
Institute for Superconducting & Electronic Materials, University of Wollongong
Innovation Campus, Wollongong, New South Wales 2500 (Australia)
E-mail: weihongl@uow.edu.au

[+] These authors contributed equally to this work.
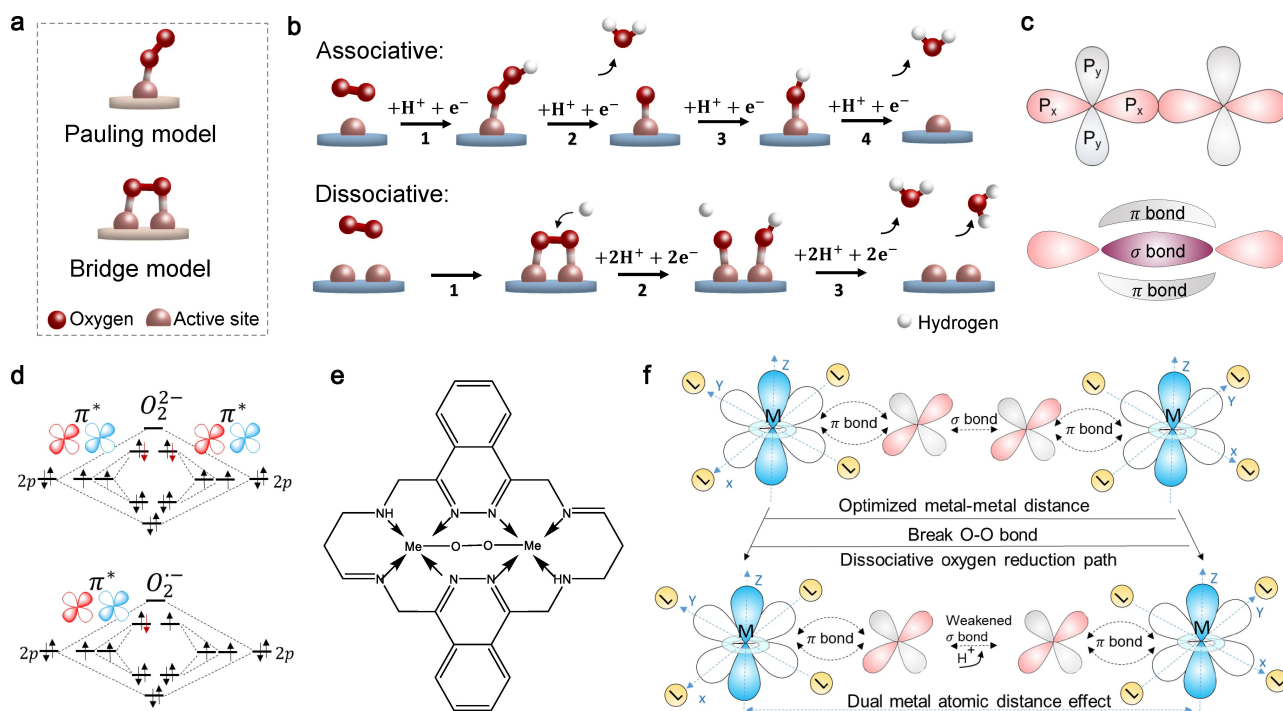
Figure 1. The mechanisms of ORR. a) Illustration of the Pauling model and the Bridge model. b) Schematic of the direct four-electron associative and dissociative ORR pathways in acid media. c) Molecular orbital diagram of an oxygen molecule. d) p-orbital diagrams of peroxide and superoxide species. e) Schematic of the O_2 adsorption model on M-M-N_x porphyrin catalysts. f) Relationship between distance effect and O—O bond breakage.

an associative or a dissociative pathway (Figure 1b). Previous studies show that the adsorption model of molecular oxygen can dominate the main reaction pathway.[10] For example, one-site oxygen adsorption, in accordance with the Pauling and Griffiths models, tends to occur via an associative path (Top, Figure 1b). Meanwhile, a dissociative mechanism is more likely to happen when the oxygen molecules are adsorbed in accordance with the bridge model (Bottom, Figure 1b). For SACs, the associative pathway is a widely recognized mechanism for the relatively low-energy hybridization orbital structure of the Pauling model and isolated single-atomic-site limitations.[11] By this pathway, however, the ORR has to start a step-by-step pathway with the rate-determining step of $O_2^*{\rightarrow}OOH^*$ (* is active site) (Figure 1b).[12] In contrast, the dissociation pathway with direct O—O splitting can achieve a direct four-electron transfer in one step and skip the sluggish kinetics of $O_2^*{\rightarrow}$ OOH^*.[11] The cleavage of O—O bridge bond also accelerates the ORR speed through the fast proton-electron transfer to another O* immediately.[13] Therefore, the dissociative pathway with fewer steps should be more efficient than the associative pathway. However, previous investigations suggest that the energy barrier for direct O—O cleavage to ensure a dissociative pathway is larger than O—OH* breakage in the associative pathway.[14] It is still a significant challenge to design active sites to decrease the energy barrier of the dissociative pathway for ORR.

The best solution to these challenges is to design a pair of active sites, such as dual atomic sites, for splitting the

O—O bond as predicted by a bridge model.[13] Hence, oxygen molecules can achieve a direct four-electron transfer in one step and circumvent the sluggish kinetics of $O_2^*{\rightarrow}OOH^*$. In addition, molecular oxygen is composed of one σ bond and one π bond, which both contribute to stabilizing the oxygen molecules (Figure 1c).[15] When more electrons are donated to π* antibonding, the favored intermediate species will tend to be peroxide (O_2^{2-}) rather than superoxide (O_2^-) because more electrons in antibonding orbitals will destabilize the interaction between oxygen atoms (Figure 1d).[16] Hence, to achieve direct O—O cleavage via the dissociative pathway, it is imperative to engineer the electron structure and geometric properties of dual active sites for electron transfer from dual active sites to oxygen atoms. Despite rising efforts in investigating carious dual SACs for ORR, the mechanism and effect study of dual atoms for ORR behavior are still in their infancy.[7b,17] Previous studies suggested that the distance of adjacent active sites can influence ORR behavior. For example, Jin et al. demonstrated that the distance effect (>5 Å) of two adjacent Fe SAs is the critical factor for site-to-site communication (electronic interaction).[1b] Collman et al. and Liu et al. reported that Co-Co-N_x porphyrins with a dual atomic Co—Co distance of ≈ 4 Å permit the rupture of the O—O bond (Figure 1e).[18] Additionally, the heterogeneous structure of the active center leads to more electron transfer and affects the ORR mechanism as well. For instance, Gong et al. proposed that N atoms neighboring carbon active sites were able to change the oxygen adsorption from the typical Pauling model to the

bridge model behavior, owing to the effective weakening of the O–O bond.[1c] Whereas, the rational design of dual active sites to achieve a simple-step dissociative mechanism has not yet been reported.

Herein, we overcome the aforementioned difficulties by developing a bi-functional ligand-assisted synthesis strategy to pre-control the atomic distance of Fe and zinc (Zn) atomic pairs on metal-organic framework (MOF)-derived carbon. The results show that this specific distance of Fe and Zn diatomic pairs (≈ 3.0 Å) can directly dissociate oxygen with low overpotential, leading to a boosted ORR activity in sulphuric acid (H_2SO_4) electrolyte. Density functional theory (DFT) calculations further proved that the dissociative pathway is successfully simplified through even-oriented charge and electron transfer, thus efficiently weakening the energy barriers of the O–O σ bond (Figure 1f). We have unraveled the kinetic behavior of paired hetero atoms originating from the distance effects, thus providing important insight into the inherent ORR mechanisms.

Results and Discussion

In the present work, the diatomic distance of Fe and Zn SAs on the MOF-derived carbon substrate is tuned by the pre-controlled coordination reaction between ligands and metal cations. Based on Lewis's Hard-Soft-Acid-Base (HSAB) theory, ammonium (–NH_2) groups prefer to form ionic bonds with hard Lewis acidic metals (like Fe^{3+} ions), while the soft Lewis base, the sulfur (S)-based groups (like -RS), tend to coordinate with soft Lewis acid and softer-borderline acid (like Zn^{2+}).[19] In addition to the distance of 3.0 Å between -RS and -NH_2 groups in thioacetamide, Fe^{3+} and Zn^{2+} ions can be precisely paired together with a distance of ≈ 3.0 Å (Figure 2a). Figure S2 shows that the mixed solution of Fe^{3+} ions and thioacetamide changes from an initial orange to a clear solution, indicating successful coordination. Then, the Fe^{3+}-thioacetamide coordination compounds were added to zeolitic imidazolate framework 8 (ZIF-8) to pair with the second metal Zn, and the product was named the precursor of Fe-Zn@SNC. The fabrication of the precursor was first confirmed by its rough surface compared with the smooth surface of the bare ZIF-8 (Figure S3). Moreover, X-ray diffraction (XRD) results show that the precursor has similar peaks with bare ZIF-8 but slightly widening to the left due to the occupation of S groups on Zn nodes (Figure S4), further confirming the expected distorted morphology as shown in Figure S3.[20] It also shows the absence of metal or metal alloy peaks, demonstrating that the introduced Fe^{3+}-thioacetamide coordination compound were well grafted on the Zn nodes of ZIF-8. X-ray photo-electron spectroscopy (XPS) results further verify that the -NH_2 groups of thioacetamide are successfully bonded with Fe^{3+} ions while the -RS groups are coordinated with the Zn nodes of ZIF-8 (Figures S5 and S6).[20] These characterizations strongly indicate that Fe and Zn are linked together successfully without metal or metal alloy formation in the precursor. It is important for forming hetero-atomic pairs with pre-designed distance. With high-temperature sintering of well-designed precursor at 900°C and subsequent leaching to remove the partially formed ZnS/$Zn_{0.8}Fe_{0.6}$S particles (Figure S7), we obtained the dual atomic Fe and Zn SACs anchored by S and N on carbon substrate (Fe-Zn@SNC) (Figure 2a).[21] Moreover, to further investigate the structural features and catalytic performance of the Fe-Zn@SNC, we synthesized three comparison samples of Fe-Zn@NC (without S), Fe@SNC (without Zn), and Zn@SNC (without Fe) (Synthesis methods of Supporting Information).
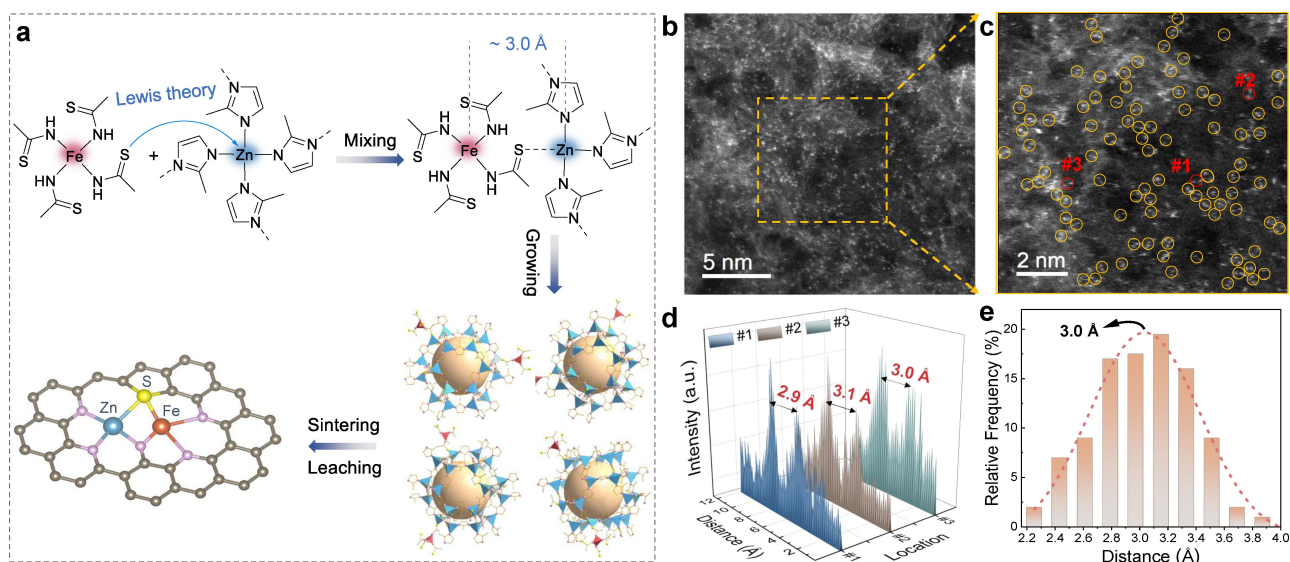

Figure 2. Preparation and characterization of Fe-Zn@SNC. a) Schematic illustration for the synthesis procedure of Fe-Zn@SNC. b) HAADF-STEM image of Fe-Zn@SNC, showing the single atoms and in-plane pores. c) The enlarged HAADF-STEM image shows the dual atoms (yellow circles) dispersed in the SNC substrate. d) Electronic intensity image around the location of #1, #2, and #3 in (c). e) Kernel method of frequency statistic and Gauss fitting of diatomic distances obtained from all the yellow circles in (c).

The S of the Fe^{3+}-thioacetamide compound partially breaks and reconstructs the initial structure of ZIF-8, leading to the final porous carbon structure after pyrolysis (Figure S8). Brunauer–Emmett–Teller (BET) and scanning transmission electron microscopy (STEM) measurements exhibit plentiful large channels and porous disorder structures formed by fractured carbon crystallites (Figures S9–S11). XRD patterns of Fe-Zn@SNC show two wide diffraction peaks at 28° and 44° indexed to carbon (002) and (101), respectively, denoting the absence of crystalline metal or metal compounds (Figure S12). The (002) diffraction peaks of Fe-Zn@SNC and Zn@SNC at 28°, which are larger than the 26° peak of graphitic carbon, indicate morphology deformity of Fe-Zn@SNC and Zn@SNC catalysts. This is in line with the intensity ratio of the D ($1345\,cm^{-1}$) and G ($1590\,cm^{-1}$) bands, as shown in Raman spectra (Figure S13), which further suggests relatively more dense defect and edge in the carbon matrix compared to non-S comparison samples.[22] The improved capability of electron conduction and mass transfer induced from such polyporous structures render more active sites for electrons and ions to access for efficient electrocatalysis. STEM energy dispersive spectroscopy (EDS) analysis further demonstrates that the elements C, N, O, S, Zn, and Fe are uniformly dispersed (Figure S14). High-angle annular dark-field STEM (HAADF-STEM) images confirm that a large amount of intense bright spots are regarded as single metal atoms due to their higher reflection electronic intensity than the surrounding non-metal elements dispersed in the carbon substrates (Figures 2b and S15). The detailed HAADF-STEM image (Figure 2c) further exhibits clear atomic pairs (yellow circles). In addition, the different reflection electronic intensities of the atomic metal pairs suggest that the adjacent bright dots are hetero Fe and Zn SAs coupled together (Figure 2d).[21a] Moreover, our statistical analysis in Figure 2e indicates that diatomic distances from 2.8 to 3.3 Å are dominant in Fe-Zn@SNC. Gauss fitting result shows that these paired atoms have the highest prevalence of atomic distances around 3.0 Å (Figure 2e). Hence, we have successfully implemented the distance pre-control strategy by using two functional groups in one small molecule to link hetero Fe and Zn atoms within the targeted distance. Previous investigations studied two distance ranges of dual atomic pairs except for our distance range. Specifically, one forms M–M bonds directly with 2.10–2.65 Å bond lengths (Table S1), and the other is two neighboring M-N_x moieties with distances larger than 4.0 Å.[1b,17,23] Hence, our work filled the gap of diatomic distance between the above two types. Furthermore, the mass loading of SAs is deemed to have a positive correlation with ORR performance. The measurement of inductively coupled plasma optical emission spectrometry (ICP-OES) determined that the mass loadings of Fe and Zn atoms are 0.80 wt % and 2.64 wt %, respectively, which is consistent with the results obtained by the XPS quantitative analysis (Table S2). The total mass loading of atomic Fe and Zn (3.44 wt %) is higher than most published dual SACs reports (Table S3), indicating that the current strategy effectively increases the mass content of diatomic sites.

X-ray near-edge structure (XANES) and XPS analysis were employed to further investigate the chemical states and coordination environments of Fe and Zn atoms in Fe-Zn@SNC.[24] The XANES spectra of Fe K-edge show that its energy absorption threshold situates midway between that of Fe_2O_3 and FeO, which matches the observation of XPS Fe $2p3$ peak located between Fe^{2+} (709.6 eV) and Fe^{3+} (711.6 eV) (Figure S16), indicating that the valence state of Fe atoms in Fe-Zn@SNC is between $+2$ and $+3$ (Figure 3a).[25] Moreover, the linear relation between the Fe valence and the pre-edge location shows that the Fe valence in Fe-Zn@SNC is around $+2.51$ (Figure 3b). Similarly, the results of XPS and Zn K-edge XANES spectra confirm that the Zn oxidation state is between 0 and $+2$ (Figures 3c and S17).[26] Interestingly, the pre-edge energy of Fe shown in Figure 3a has a negative energy shift relative to the isolated Fe-N_4 moieties in FePc, demonstrating the increment of Fe valence in Fe-Zn@SNC. Conversely, the inset in Figure 3c exhibits a decreased adsorption edge of Zn compared with Zn-N_4 species in ZnPc. The valence changes align with energy shifts of XPS spectra (Figures S16–S20), which further confirms that Fe atoms donate partial electrons to Zn. Furthermore, from Figure S16, the binding energy in S $2p3$ spectra of Fe-Zn@SNC shifts to lower energy by -0.28 eV than that in Zn@SNC, but higher $+0.59$ eV than that in Fe@SNC, indicating that S atoms donate electrons to Fe atoms and obtain electrons from Zn atoms. The interaction between three atoms might be the engine to force the formation of Fe–Zn pairs coordinated with S.[23]

The structure of Fe-Zn@SNC is verified by comprehensive analysis and fitting of the extended XAFS (EXAFS) spectrum. The k^2-weighted Fourier transform EXAFS (FT-EXAFS) spectrum of Fe atoms in Fe-Zn@SNC displays a central peak around 1.45 Å, which is longer than the Fe–N peak at 1.35 Å and shorter than the Fe–S peak at 1.49 Å bond (Figure 3d), and thus can be considered as the backscattering between Fe with N and S light atoms. No strong signal is seen at 2.2 Å, which is a characteristic peak of metallic Fe. Similar observations in Zn FT-EXAFS of Fe-Zn@SNC exhibit similar N and S coordination features without Zn–Zn bonds (Figure 3e). Moreover, EXAFS wavelet transforms (WTs) analysis for Fe and Zn atoms in Fe-Zn@SNC, and metal foils (Fe foil and Zn foil) confirm that only one intensity maximum exists in each case, further demonstrating that Fe and Zn disperse atomically in Fe-Zn@SNC (Figure 3f, g).[27] Moreover, quantitative least-squares EXAFS fitting analysis of Zn uncovers that Zn SAs are coordinated by three N and one S atoms with Zn–N and Zn–S bond lengths of 2.04 Å and 2.34 Å, forming the Zn-N_3S_1 configuration (Figures 3h, S21, S22, and Table S4). Similarly, the coordination numbers of the N and S atoms in the first shell of Fe SAs are 2.7 and 1.3, with bond lengths of 1.93 and 2.22 Å, respectively. In addition, the second coordination sphere by one Fe–Zn bond at 2.98 Å and several Fe–C bonds are demonstrated (Figures 3i, S23, S24, and Table S5), in line with the above Fe–Zn distance observation of HAADF-STEM analysis. All these results confirm that the Fe and Zn are atomically dispersed and paired together with the FeN3–S–ZnN3 structure (the inset
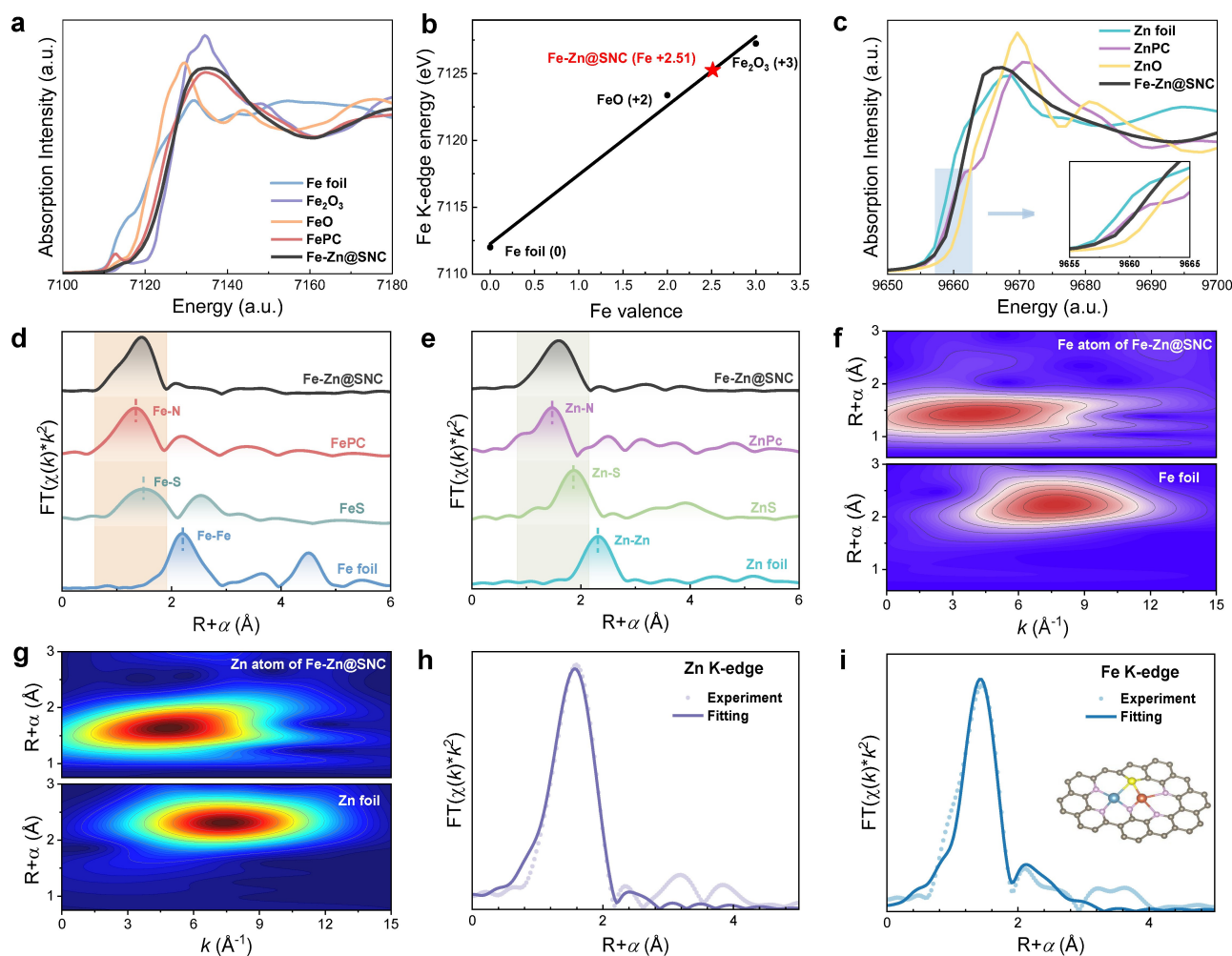
Figure 3. Atomic structure characterization. a) Fe K-edge XANES. b) Liner fitting for Fe valences in Fe-Zn@SNC, Fe_2O_3, FeO, and Fe foil derived from corresponding Fe K-edge XANES spectra. c) Zn K-edge XANES, where the magnified energy adsorption diagram is inserted. d) k^2-weighted FT-EXAFS spectra of Fe K-edge. e) Same as d, but with Zn K-edge. f) WTs for k^2-weighted Fe K-edge EXAFS of Fe-Zn@SNC and Fe foil. g) Same as f, but with Zn atom and Zn foil. h) EXAFS spectra fitting of Zn in Fe-Zn@SNC. i) Same as h, but fitting for Fe atoms, where the inset shows the optimal configuration by DFT calculation.

in Figure 3i). It is notable that the S atoms work as a key component to stretch the Fe and Zn SAs because the lower electronegativity of S than N induces a longer bond with metal atoms.[28]

The ORR performances of all catalysts were evaluated using a rotating ring-disk electrode with immobilized target electrocatalysts on its glassy-carbon disk in O_2-saturated 0.5 M H_2SO_4. The Fe-Zn@SNC exhibits an obvious cyclic voltammetry (CV) reduction peak at 0.83 V versus the reversible hydrogen electrode (V_{RHE}), which is absent in the N_2-saturated electrolyte (Figure S25). This result indicates an outstanding ORR catalytic capability of Fe-Zn@SNC. Figure 4a shows the polarization curves of Fe-Zn@SNC, Fe–Zn@NC, Fe@SNC, Zn@SNC, and 20% Pt/C. It is evident that the linear sweep voltammetry (LSV) of Fe-Zn@SNC achieves the highest onset potential (E_{onset}) of 0.99 V_{RHE} and half-wave potential ($E_{1/2}$) of 0.86 V_{RHE} among the benchmark of 20% Pt/C with E_{onset} of 0.93 V and $E_{1/2}$ of 0.81 V_{RHE}, and other reference samples (Figure 4b). Further-

more, the Fe-Zn@SNC catalyst presents a high ORR limiting current density (J_L) of 5.4 mA cm^{-2}, which is greater than that of Pt/C (4.6 mA cm^{-2}). The ORR kinetic current density (J_K) of Fe-Zn@SNC at 0.85 V_{RHE} is estimated as 5.17 mA cm^{-2}, surpassing Pt/C with J_K of 0.84 mA cm^{-2} and the other comparison samples (Figure 4b). The lowest Tafel slope of Fe-Zn@SNC (64 mV dec^{-1}) further evidences its highly efficient ORR kinetics compared with the benchmark and comparison samples (Figure 4c).

The Koutecky–Levich plots at different rotating speeds (Figures 4d and S26) and the rotating ring-disk electrode (RRDE) measurement (Figure 4e) demonstrate that the Fe-Zn@SNC has a stable electron transfer number (n) with calculated and experimental results of four, consisting to a low 5% H_2O_2 yield. Methanol tolerance and stability are the challenges in developing practical catalysts for fuel cells. Figure 4f shows the methanol tolerance of Fe-Zn@SNC measured in chronoamperometry after injecting 0.5 M methanol, indicating that Fe-Zn@SNC displays a strong
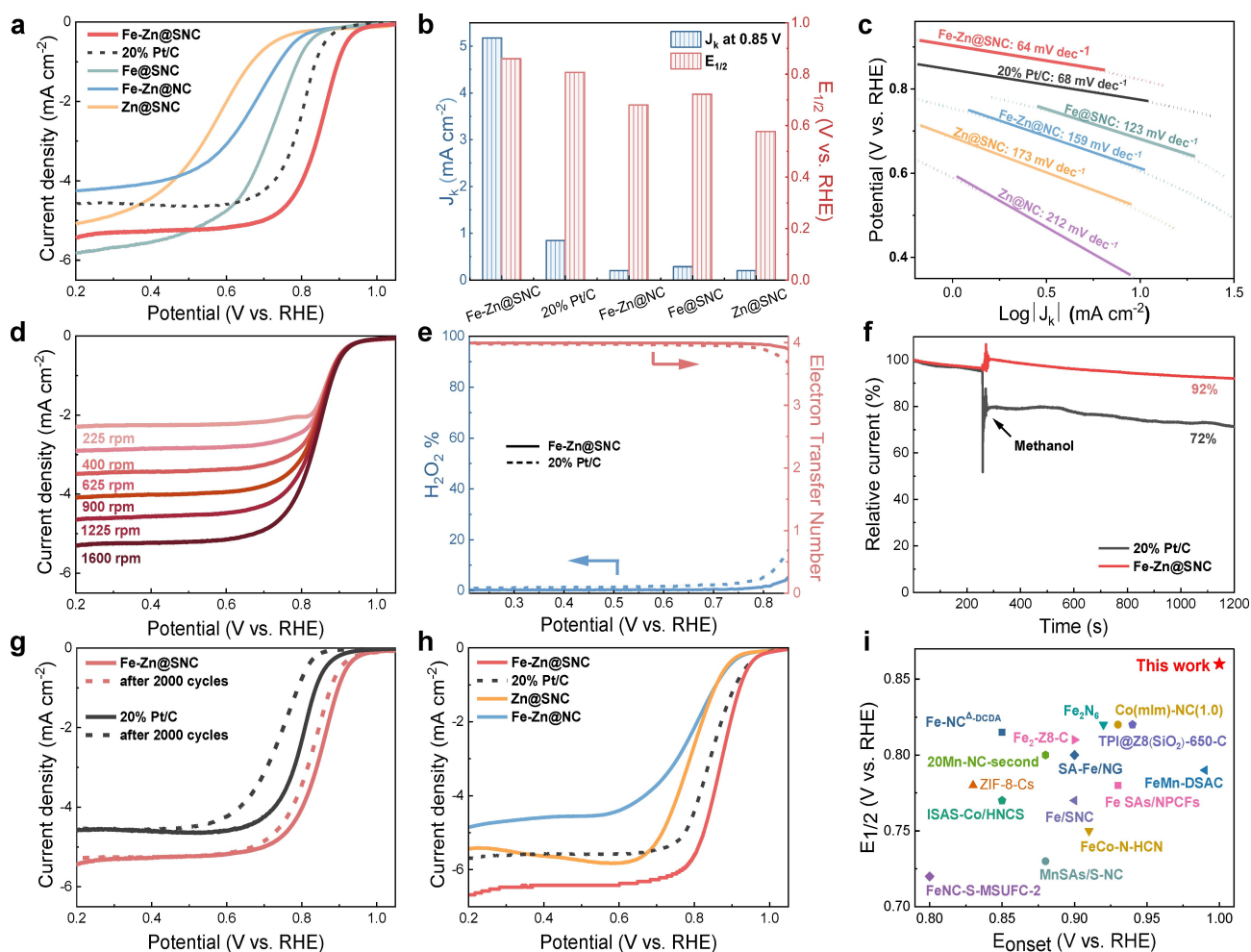
Figure 4. ORR performance. a) LSV curves in O_2-saturated 0.5 M H_2SO_4 at a sweep rate of 5 mV s^{-1} and a rotation rate of 1600 rpm. b) Comparison of kinetic current density at 0.85 V_{RHE} and $E_{1/2}$. c) Tafel plots. d) ORR polarization LSV curves of Fe-Zn@SNC at different rotation rates. e) The yield of H_2O_2 and electron transfer number of Fe-Zn@SNC and 20% Pt/C as a function of potential. f) Methanol tolerance. g) Stability of RDE polarization curves of Fe-Zn@SNC before and after 2000 potential cycles. h) LSV curves in O_2-saturated 0.1 M KOH. i) Comparison of E_{onset} and $E_{1/2}$ between Fe-Zn@SNC and other recently published carbon-based SACs in 0.5 M H_2SO_4.

methanol tolerance with 30% higher current retention of ORR activity than that of 20% Pt/C. Figure 4g shows the good durability of Fe-Zn@SNC valued by CV measurement at a sweep rate of 100 mV s^{-1}. After 2000 continuous cycles, only a 25 mV change in $E_{1/2}$, which is smaller than a 59 mV change in Pt/C. This clearly indicates that the Fe-Zn@SNC has enhanced stability compared to 20% Pt/C. Furthermore, Fe-Zn@SNC exhibits a good ORR performance of 0.87 V_{RHE} half-wave potential in 0.1 M potassium hydroxide (KOH) electrolyte (Figure 4h). Figure S27a–f demonstrates the detailed ORR performance in 0.1 M KOH media, suggesting its empirical ORR performance in both acidic and alkaline electrolytes. The outstanding ORR performance of Fe-Zn@SNC stands above previous reports (Figure 4i and Table S3).
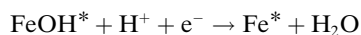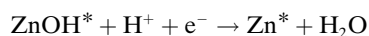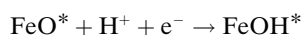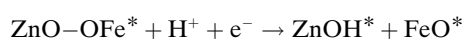
The superior ORR performance of Fe-Zn@SNC indicates that the designed Fe and Zn diatomic pairs with such a suitable distance range are critical for the electrochemical reduction of oxygen molecules through a pathway of direct O–O bond cleavage. DFT calculations have been conducted

to gain a further understanding of the relationship between Fe–Zn distance and boosted ORR activities. There are two mechanisms of several models based on Fe-Zn@SNC (Figure S28) with different Fe–Zn distances ranging from 2.60 to 3.50 Å. The clear reaction pathways and calculated free energy in Figure 5a show the direct O–O bond cleavage happened on the model of Fe-Zn@SNC with 3.16 Å Fe–Zn distance (abbreviated as 3.16 Å model), while the sluggish associative pathway is for 2.64 Å and 3.46 Å models (Figure S29). It is interesting that the adsorption models of oxygen and corresponding ORR pathways have been changed by varying the distance between Fe and Zn atoms. In this case, as informed by our calculations, the more favorable dissociative reaction process (direct O–O bond cleavage pathway) is proposed below (note: steps 2 and 3 are simultaneous):

$$Zn-Fe^* + O_2 \rightarrow ZnO-OFe^* \qquad (0)$$
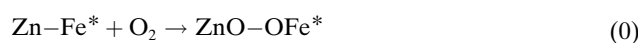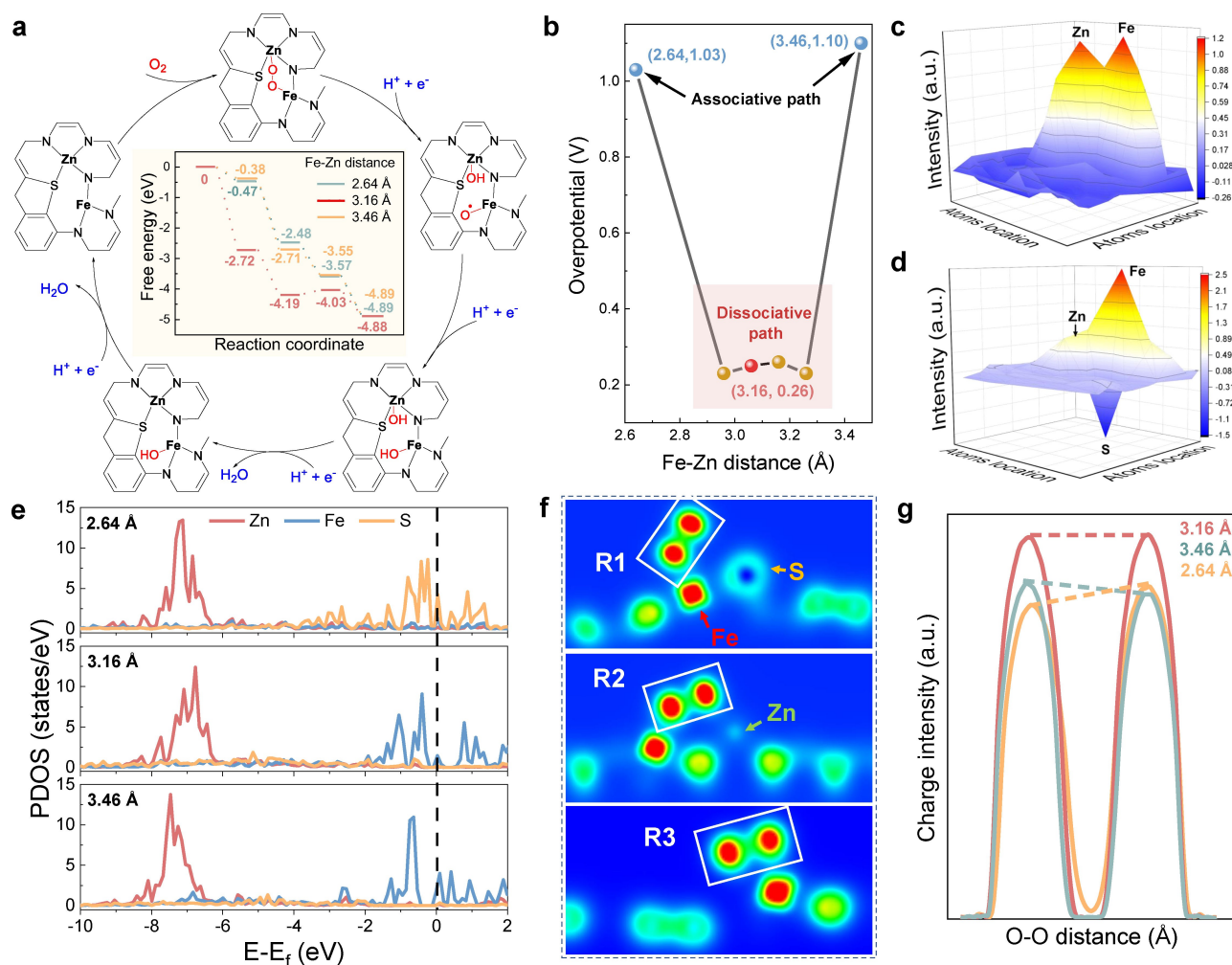
Figure 5. Reaction mechanism and distance effects investigation. a) ORR mechanism pathways and free energy of Fe-Zn@SNC models for different Fe—Zn distances of 3.16 Å. b) Overpotential of Fe-Zn@SNC models with different Fe—Zn distances from 2.60 to 3.50 Å. c), d) Barder charge of Fe-Zn@SNC models with Fe—Zn distances of 3.16 (c) and 2.46 Å (d). e) PDOS with the distance of Fe—Zn at 2.64 Å, 3.16 Å, and 3.46 Å, where the broken line means Femi level. f) Electron distribution of O_2^* (white box) absorbed on the surface of three Fe-Zn@SNC models (R1: 2.64 Å, R2: 3.16 Å, R3: 3.46 Å). g) Total charge transfer between O_2^* and Fe—Zn bridge site of three Fe-Zn@SNC models (2.64 Å, 3.16 Å, and 3.46 Å).

$$ZnO-OFe^* + H^+ + e^- \rightarrow ZnOH^* + FeO^* \tag{1}$$

$$FeO^* + H^+ + e^- \rightarrow FeOH^* \tag{2}$$

$$ZnOH^* + H^+ + e^- \rightarrow Zn^* + H_2O \tag{3}$$

$$FeOH^* + H^+ + e^- \rightarrow Fe^* + H_2O \tag{4}$$

Theoretical ORR overpotential values of these models from 2.60 to 3.50 Å were estimated. Figure 5b shows that direct O–O bond cleavage mechanism only occurs as the distance is in the range of 2.88 to 3.26 Å with a fairly low overpotential of less than 0.3 eV, corresponding to the ORR experimental results. To assess the distance effect for electron and charge behavior, we performed the Bader charge and projected density of states (PDOS) for 2.64 Å, 3.16 Å, and 3.64 Å models. Figure 5c shows the balanced Bader charge of the 3.16 Å model, which facilitates the oxygen molecule to adsorb as described by the bridge

model, different from the uneven Fe–Zn charge transfer in the 2.64 Å model (Figure 5d). Moreover, the PDOS of Fe atoms in 3.16 and 3.46 Å models is above the Fermi level (Figure 5e), indicating that Fe and Zn sites are sensitive to ORR intermediates adsorption or desorption. The maximum peak of Zn PDOS in the 3.16 Å model is up-shifted compared with the 3.46 models, suggesting Zn atoms in the 3.16 Å model have more activated electrons to react with intermediates. In contrast, in the 2.64 model, d electrons of S atoms substitute Fe and occupy near the Fermi level. It means the activated electrons are from S, which can prevent oxygen adsorb, so O_2 is adsorbed by the Pauling model. Furthermore, in the 3.16 model, the Fe peaks replace S peaks, and the intensity of Zn peaks becomes weaker than in the 2.64 models, which means electron and charge transfer from S atoms to Zn SAs. Such results coincide with the electron transfer behavior from experimental XPS and XAFS analysis (Figures 3a, c, and S16–S20). To further explore the oxygen adsorption behavior, which is the key

factor of the dissociative mechanism, we estimated electron distributions of O_2^* (R1–3) absorbed on the surface of Fe–Zn sites in three models (Figure 5f). The extracted profile of the corresponding oxygen molecules indicates that the Fe–Zn sites in the 3.16 Å model possess the highest and the most balanced electron intensity, meaning that oxygen molecules have the strongest interaction with 3.16 Å Fe–Zn dual sites (Figure 5g). Hence, the changes in the electron transfer mechanism could potentially weaken σ bonding and reduce the splitting energy of O–O bond (Figure S30). Impressively, we noticed that the bridge model behavior is preferred with a larger total charge transfer than that given by the Pauling model (Figure 5g). The equivalent interaction with two oxygen atoms has two electrons filled in the antibonding of oxygen orbitals, which boosts O–O bond cleavage. In contrast to the balanced charge distribution, the single charge peak can only enable one-site electron donation to oxygen such that the oxygen reduction can at best proceed via an associative pathway.

To experimentally explore the nature of the electronic structures of catalytic units together with the reduced oxygen species, we adopt ex-situ soft X-ray absorption spectra (SXAS) to investigate the electrocatalytic-processed Fe-Zn@SNC catalysts that were obtained after stability reactions at different voltages from 1.0 V to 0.3 V. It is known that SXAS signals are sensitive to electron distributions at alterable energy levels, which are able to explain electron-transfer phenomenon between Fe-Zn@SNC catalyst and oxygen species during the ORR process.[29] The O K-edge curves possess two main peaks in Figure S31. The pre-edge peaks at ≈532 eV correspond to the excitation from O 1s electrons to the unoccupied hybridized state of Fe 3d with O 2p orbitals (Fe–O), whilst the higher-energy wider peak at ≈540 eV can be assigned to O 2p-Zn 4s hybridizations (Zn–O).[30] The normalized areas of Fe–O peaks (Figure S32a) show reduction along with the ORR process, indicating an increase of electrons transfer to the O 1p band (Figure S32b).[31] Also, the normalized Fe L_3-edge peaks in Figure S33a exhibit higher energy shifts over the different voltage tests, which further determined that Fe SAs donate electrons to oxygen.[32] A similar electron-transfer pathway (M→O) for Zn SAs and O atoms can be proved (Figures S31 and S34).[28,30b] These phenomena congruously implied that Fe and Zn SAs synergistically contribute electrons to unoccupied oxygen orbital levels, resulting in fast cleavage of oxygen bonds. Interestingly, the peak intensity of Fe–O and Zn–O in O K-edge SXAS is the lowest at 0.9 V, suggesting that the electron transfer occurs at the early stage of ORR. These observations corroborated the experimental electrochemical results and DFT calculations, showing strong evidence for our proposed ORR pathway of the Fe-Zn@SNC electrocatalyst.

Conclusion

In summary, we have developed a bi-functional ligand-assisted synthesis method to precisely regulate the diatomic distance of Fe and Zn atoms on carbon substrates based on the HSAB theory. The resultant Fe-Zn@SNC catalyst has paired Fe and Zn atoms with ≈3.0 Å distances in the FeN_3-S-ZnN_3 configuration. The atomic distance of Fe–Zn atomic pairs is crucial for achieving excellent ORR performance in both acidic and alkaline electrolytes. Our results show that Fe–Zn sites with a distance range from 2.88 to 3.26 Å endow a balanced charge intensity to interact with the antibonding of oxygen atoms strongly. These distance effects destabilize the O–O bond and finally induce a dissociative ORR pathway. The dissociative ORR pathway overcomes the high energy barriers of the direct dissociation of O–O bonds and avoids the rate-determining step $O_2^* \rightarrow OOH^*$. The rational atomic structure design of catalysts and streamlined resultant ORR pathway play key roles in achieving fast kinetics and low overpotentials for ORR. This work opens a new avenue for developing high-performance catalysts based on atomic structure design.

Conflict of Interest

The authors declare no conflict of interest.

Data Availability Statement

Research data are not shared.

Keywords: Acid Electrolytes · Dissociative Mechanism · Distance Effect · Dual-Atomic Structure Engineering · Oxygen Reduction Reaction

[1] a) L. Bu, N. Zhang, S. Guo, X. Zhang, J. Li, J. Yao, T. Wu, G. Lu, J.-Y. Ma, D. Su, *Science* **2016**, *354*, 1410–1414; b) Z. Jin, P. Li, Y. Meng, Z. Fang, D. Xiao, G. Yu, *Nat. Catal.* **2021**, *4*, 615–622; c) K. Gong, F. Du, Z. Xia, M. Durstock, L. Dai, *Science* **2009**, *323*, 760–764.

[2] a) A. Appleby, *J. Electroanal. Chem.* **1993**, *357*, 117–179; b) S. Basu, *Recent Trends in Fuel Cell Science and Technology [electronic Resource]*, Springer, Cham, **2007**.

[3] a) J. Shui, M. Wang, F. Du, L. Dai, *Sci. Adv.* **2015**, *1*, e1400129; b) P. Chen, L. K. Wang, G. Wang, M. R. Gao, J. Ge, W. J. Yuan, Y. H. Shen, A. J. Xie, S. H. Yu, *Energy Environ. Sci.* **2014**, *7*, 4095–4103.

[4] R. Jasinski, *J. Electrochem. Soc.* **1965**, *112*, 526.

[5] C. W. Bezerra, L. Zhang, K. Lee, H. Liu, A. L. Marques, E. P. Marques, H. Wang, J. Zhang, *Electrochim. Acta.* **2008**, *53*, 4937–4951.

[6] a) Y. Feng, N. Alonso-Vante, *Phys. Status Solidi B* **2008**, *245*, 1792–1806; b) M. Anantharaman, S. Saravanan, M. C. Joseph, S. Venkitachalam, P. Prabhakaran, *J. Appl. Phys.* **2003**, *91*, 2529–2535.

[7] a) Y. He, S. Liu, C. Priest, Q. Shi, G. Wu, *Chem. Soc. Rev.* **2020**, *49*, 3484–3524; b) C. X. Zhao, B. Q. Li, J. N. Liu, Q. Zhang, *Angew. Chem. Int. Ed.* **2021**, *60*, 4448–4463; *Angew. Chem.* **2021**, *133*, 4496–4512; c) D. Zhao, Z. Zhuang, X. Cao, C. Zhang, Q. Peng, C. Chen, Y. Li, *Chem. Soc. Rev.* **2020**, *49*, 2215–2264.

[8] a) A. Kulkarni, S. Siahrostami, A. Patel, J. K. Norskov, *Chem. Rev.* **2018**, *118*, 2302–2312; b) Y. Wang, H. Su, Y. He, L. Li, S. Zhu, H. Shen, P. Xie, X. Fu, G. Zhou, C. Feng, D. Zhao, F. Xiao, X. Zhu, Y. Zeng, M. Shao, S. Chen, G. Wu, J. Zeng, C. Wang, *Chem. Rev.* **2020**, *120*, 12217–12314.

[9] a) E. Yeager, *Electrochim. Acta* **1984**, *29*, 1527–1537; b) L. Pauling, *Nature* **1964**, *203*, 182–183; c) J. Griffith, *Proc. R. Soc. London Ser. A* **1956**, *235*, 23–36.

[10] R. Adžić, J. Wang, *J. Phys. Chem. B* **1998**, *102*, 8988–8993.

[11] Z. W. Seh, J. Kibsgaard, C. F. Dickens, I. Chorkendorff, J. K. Norskov, T. F. Jaramillo, *Science* **2017**, *355*, eaad4998.

[12] I. Morcos, E. Yeager, *Electrochim. Acta.* **1970**, *15*, 953–975.

[13] L. Zhong, S. Li, *ACS Catal.* **2020**, *10*, 4313–4318.

[14] a) E. López-Chávez, A. Garcia-Quiroz, G. González-García, Y. A. Peña-Castañeda, J. A. I. Díaz-Góngora, F. de Landa Castillo-Alvarado, *Int. J. Hydrogen Energy* **2016**, *41*, 23281–23286; b) C. Zhang, J. Sha, H. Fei, M. Liu, S. Yazdi, J. Zhang, Q. Zhong, X. Zou, N. Zhao, H. Yu, *ACS Nano* **2017**, *11*, 6930–6941.

[15] G. Henrici-Olivé, S. Olivé, *Angew. Chem. Int. Ed. Engl.* **1974**, *13*, 29–38; *Angew. Chem.* **1974**, *86*, 1–12.

[16] R. Chang, *Physical chemistry for the biosciences*, University Science Books, Sausalito, **2005**.

[17] M. Wang, S. Lu, X. Wu, J.-P. Veder, B. Johannessen, L. Thomsen, J. Zhang, S.-z. Yang, *Appl. Catal. B* **2021**, *284*, 119717.

[18] a) J. P. Collman, M. Marrocco, P. Denisevich, C. Koval, F. C. Anson, *J. Electroanal. Chem. Interfacial Electrochem.* **1979**, *101*, 117–122; b) H. Liu, M. J. Weaver, C. Wang, C. Chang, *J. Electroanal. Chem. Interfacial Electrochem.* **1983**, *145*, 439–447.

[19] T.-L. Ho, *Chem. Rev.* **1975**, *75*, 1.

[20] a) Y. Chen, S. Ji, S. Zhao, W. Chen, J. Dong, W. C. Cheong, R. Shen, X. Wen, L. Zheng, A. I. Rykov, S. Cai, H. Tang, Z. Zhuang, C. Chen, Q. Peng, D. Wang, Y. Li, *Nat. Commun.* **2018**, *9*, 5422; b) H. Shen, E. Gracia-Espino, J. Ma, K. Zang, J.

Luo, L. Wang, S. Gao, X. Mamat, G. Hu, T. Wagberg, S. Guo, *Angew. Chem. Int. Ed.* **2017**, *56*, 13800–13804; *Angew. Chem.* **2017**, *129*, 13988–13992.

[21] a) M. Liu, N. Li, S. Cao, X. Wang, X. Lu, L. Kong, Y. Xu, X. H. Bu, *Adv. Mater.* **2022**, *34*, 2107421; b) J. Zhang, Y. Zhao, C. Chen, Y. C. Huang, C. L. Dong, C. J. Chen, R. S. Liu, C. Wang, K. Yan, Y. Li, G. Wang, *J. Am. Chem. Soc.* **2019**, *141*, 20118–20126.

[22] X. Zhu, D. Zhang, C.-J. Chen, Q. Zhang, R.-S. Liu, Z. Xia, L. Dai, R. Amal, X. Lu, *Nano Energy* **2020**, *71*, 104597.

[23] L. Jiao, J. Zhu, Y. Zhang, W. Yang, S. Zhou, A. Li, C. Xie, X. Zheng, W. Zhou, S. H. Yu, H. L. Jiang, *J. Am. Chem. Soc.* **2021**, *143*, 19417–19424.

[24] a) H. Li, K. Du, C. Xiang, P. An, X. Shu, Y. Dang, C. Wu, J. Wang, W. Du, J. Zhang, S. Li, H. Tian, S. Wang, H. Xia, *J. Mater. Chem. A* **2020**, *8*, 17136–17149; b) D. Liu, B. Wang, H. Li, S. Huang, M. Liu, J. Wang, Q. Wang, J. Zhang, Y. Zhao, *Nano Energy* **2019**, *58*, 277–283; c) Y. Pan, S. Liu, K. Sun, X. Chen, B. Wang, K. Wu, X. Cao, W. C. Cheong, R. Shen, A. Han, Z. Chen, L. Zheng, J. Luo, Y. Lin, Y. Liu, D. Wang, Q. Peng, Q. Zhang, C. Chen, Y. Li, *Angew. Chem. Int. Ed.* **2018**, *57*, 8614–8618; *Angew. Chem.* **2018**, *130*, 8750–8754.

[25] Q. Li, W. Chen, H. Xiao, Y. Gong, Z. Li, L. Zheng, X. Zheng, W. Yan, W. C. Cheong, R. Shen, N. Fu, L. Gu, Z. Zhuang, C. Chen, D. Wang, Q. Peng, J. Li, Y. Li, *Adv. Mater.* **2018**, *30*, 1800588.

[26] J. Wang, H. Li, S. Liu, Y. Hu, J. Zhang, M. Xia, Y. Hou, J. Tse, J. Zhang, Y. Zhao, *Angew. Chem. Int. Ed.* **2021**, *60*, 181–185; *Angew. Chem.* **2021**, *133*, 183–187.

[27] M. Qiao, Y. Wang, Q. Wang, G. Hu, X. Mamat, S. Zhang, S. Wang, *Angew. Chem. Int. Ed.* **2020**, *59*, 2688–2694; *Angew. Chem.* **2020**, *132*, 2710–2716.

[28] R. T. Sanderson, *J. Am. Chem. Soc.* **1983**, *105*, 2259–2261.

[29] F. Frati, M. O. Hunault, F. M. De Groot, *Chem. Rev.* **2020**, *120*, 4056–4110.

[30] a) Q. Yin, J. Luo, J. Zhang, L. Zheng, G. Cui, J. Han, D. O'Hare, *J. Mater. Chem. A* **2020**, *8*, 12548–12555; b) J. Suntivich, W. T. Hong, Y.-L. Lee, J. M. Rondinelli, W. Yang, J. B. Goodenough, B. Dabrowski, J. W. Freeland, Y. Shao-Horn, *J. Phys. Chem. C* **2014**, *118*, 1856–1863; c) J.-Y. Lee, J.-W. Kim, M.-K. Lee, H.-J. Shin, H.-T. Kim, S.-M. Park, *J. Electrochem. Soc.* **2004**, *151*, C25.

[31] B. Li, H. Yan, Y. Zuo, D. Xia, *Chem. Mater.* **2017**, *29*, 2811–2818.

[32] M. Giménez-Marqués, E. Bellido, T. Berthelot, T. Simón-Yarza, T. Hidalgo, R. Simón-Vázquez, Á. González-Fernández, J. Avila, M. C. Asensio, R. Gref, *Small* **2018**, *14*, 1801900.